



HAL
open science

Use of a 6-axis robot and ink piezo-jetting to print conductive paths on 3D objects. Printed circuit geometry, and conductivity predictive model

Gioia Furia, Fanny Tricot, Didier Chaussy, Philippe Marin, Andrea Graziano,
Davide Beneventi

► To cite this version:

Gioia Furia, Fanny Tricot, Didier Chaussy, Philippe Marin, Andrea Graziano, et al.. Use of a 6-axis robot and ink piezo-jetting to print conductive paths on 3D objects. Printed circuit geometry, and conductivity predictive model. CIRP Journal of Manufacturing Science and Technology, 2021, 35, pp.855-863. 10.1016/j.cirpj.2021.09.012 . hal-03440231

HAL Id: hal-03440231

<https://hal.science/hal-03440231>

Submitted on 22 Nov 2021

HAL is a multi-disciplinary open access archive for the deposit and dissemination of scientific research documents, whether they are published or not. The documents may come from teaching and research institutions in France or abroad, or from public or private research centers.

L'archive ouverte pluridisciplinaire **HAL**, est destinée au dépôt et à la diffusion de documents scientifiques de niveau recherche, publiés ou non, émanant des établissements d'enseignement et de recherche français ou étrangers, des laboratoires publics ou privés.

USE OF A 6-AXIS ROBOT AND INK PIEZO-JETTING TO PRINT CONDUCTIVE PATHS ON 3D OBJECTS. PRINTED CIRCUIT GEOMETRY, AND CONDUCTIVITY PREDICTIVE MODEL.

*Gioia Furia^a, Fanny Tricot^a, Didier Chaussy^a, Philippe Marin^b, Andrea Graziano^a, Davide Beneventi^{*a}*

^a Univ. Grenoble Alpes, CNRS, Grenoble INP,[‡] LGP2, F-38000 Grenoble, France

^b Univ. Grenoble Alpes, CNRS, Grenoble INP,[‡] G-SCOP, F-38000 Grenoble, France

[‡] Institute of Engineering Univ. Grenoble Alpes

Corresponding author

*E-mail: davide.beneventi@pagora.grenoble-inp.fr

ABSTRACT

This paper presents an off-line programming approach for the automatic generation of trajectories and the printing program for a 6-axis robot in order to print accurate conductive paths on 3D objects using a silver microparticle solvent-based ink.

The aim of this study was to develop a semi-predictive model in order to

- Adapt the printing parameters of a 6-axis robot arm and a piezo jetting print head to the printing speed and substrate type.
- Print 3D electronic circuits matching the targeted geometry and conductivity.

For the jetting printing process, 2D patterns printed on substrates with different roughness and wettability were analysed as a function of the print head translation speed and jetting frequency which were used as base variables used to develop correlations in order to predict line width, thickness and conductivity.

The model was based on the assumption that the behaviour of a single drop impacting the printing substrate is close to that of a train of drops (i.e. lines). Thus, the diameter of individual drops on a specific substrate was used to account for support properties and jetting conditions. The study also proposes a methodology to tune the circuit morphology by adapting the jetting parameters as a function of the trajectory and the speed of the 6-axis robot.

As a representative case study, a 3D circuit was printed on a disposable paper cup obtaining an excellent agreement between measured and predicted conductivity values.

KEYWORDS

Six-axis robot, Jetting, Printed electronics, Lines morphology, Conductivity.

INTRODUCTION

Industrial robots, additive manufacturing processes, and direct writing techniques are attracting an ever increasing interest for printed electronics as they are flexible, lower the fabrication costs, decrease waste, and open new perspectives in design and integration of electronic devices.¹⁻³

Among the available direct writing technologies, the conventional ink jet and paste piezo jetting allow a high precision for dispensing of a wide variety of functional inks, i.e. from conductive, photoelectric, and dielectric inks to the solder pastes necessary for the manufacturing of printed electronic boards.^{4,5} More recently, even generating printing patterns with edge definition lower than ink jet and piezo jetting, aerosol jetting have been also identified as fast and reliable technique to print thin conductive ink layers.⁶

Despite their high performance, most of the time those contactless deposition processes are implemented on 3- or 3+1-axis Cartesian robots, which limits their use for 2D or 2.5D substrates.⁷⁻⁹ Over the years, poly articulated 6-axis robots have been intensively used in the automotive and pharmaceutical industries for localised fluid dispensing. Nevertheless, their use in high-precision freeform printing is still marginal. The reason is that the intrinsic low accuracy in the predictive control of smoothness and tool head speed in 3D trajectories requires the development of a multivariable process control approach based on 6-axis robot kinematics, printing head parameters, and targeted electronic properties.⁹

In addition, some inaccuracy sources have been identified in various studies related to the use of 6-axis robots in manufacturing processes such as painting and welding.

These inaccuracies can be due to the following reasons:

- The object geometry, which can be a macro-geometrical default or a positioning default between the object and the robot. Thus, a trajectory designed from a theoretical geometry and position is not necessarily valid. A possible solution is to scan the object to obtain a real numeric representation of the geometry and the right position.^{11,12}

- The constraints imposed on the process, which, if not well controlled, can lead to defaults in printing.¹³¹⁴
- The robot static accuracy, which can be estimated and improved with a calibration methodology.¹⁵⁻¹⁷

Moreover, in the field of electronic printing, it is important to control the fidelity between the model circuit design and the printed circuit. The performance of printed electronic circuits and components is highly dependent on the geometrical and morphological characteristics of the printed pattern. Thus, the printed lines must be narrow, smooth, even, straight, and as close as possible to attain a high specific line density and circuit integration.

Hence, the need for a good understanding and accurate control of the robot speed, line morphology, minimum width, spacing, and notch.

MATERIAL AND METHODS

Printing cell

Hardware. An in-house developed robotic cell was used in this study. The cell is composed of a STAUBLI TX2 60 6-axis robot (670 mm range and repeatability of 20 μm) equipped with a piezo jetting dispensing valve (Vermes MDV 3200A) mounting a 100 μm nozzle and a laser distance sensor (Micro-Epsilon optoNCDT 1420-100).

Figure 1a illustrates the behaviour of the valve and the parameters that can be adjusted. In this study, the valve duty cycle EL, was set to the recommended factory values (i.e. Rising RI = 0.5 ms, Open OT = 2 ms, and Falling FA = 0.2 ms). The delay time (DL) was varied between 1000 and 0.1 ms in order to tune the dispensing frequency between 1 and 350 Hz. Depending on the jetting frequency (DL) and the printhead translation speed, ejected droplet trains can form individual dots or superpose to form continuous lines as illustrated in Figure 1b.

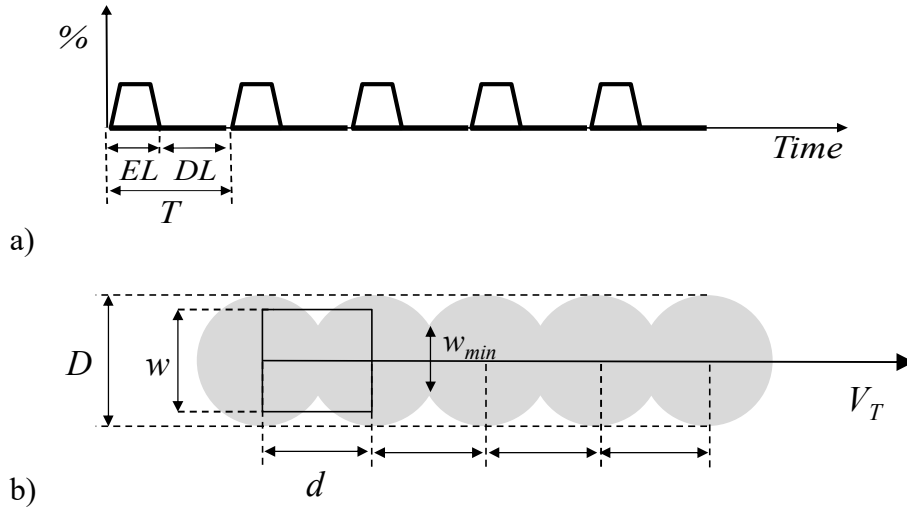


Figure 1. (a) Pulse sequence of the piezo jetting head and (b) corresponding ink drop ejected and deposited on a flat substrate. EL and DL are the drop ejection and rest time, D is the deposited drop diameter, d the distance between adjacent deposited drop and w the average width of the deposited path. V_T is the print head translation speed.

Software. The programming environment used in this study was composed by a commercial CAD software, Rhinoceros 3D (Robert McNeel & Associates), and two additional plugins, i.e. Grasshopper and RhinoRobot. Grasshopper is a visual programming language and environment that runs within the Rhinoceros 3D application and RhinoRobot (Kinematic) is a robotic simulation and off-line programming plugin for Rhinoceros 3D. It is an open software operating with Grasshopper.

As a first step to customise the RhinoRobot simulation environment, 3D models of each tool were created and implemented in the 3D environment. The Vermes Jetting 3D model was positioned on axis 6 in the x direction of the flange reference frame. The second step was the off-line programming, i.e. the development of a Stäubli VAL3 language program to automatically create robotic printing programs from the 3D trajectory. The point coordinates were obtained from RhinoRobot kinematics and were integrated in the programs.

All codes were implemented to automatically set in the program the:

- serial connection initialisation,
- tool On/Off switch,
- jetting printing parameters, i.e. number of drops and delay.

In 6-axis robots, the accurate control of joints angular speed to translate the printing head with a constant velocity over a 3D substrate struggles with speed fluctuations which are dictated by the trajectory design, target speed, and blend parameters.

Owing to a minimum refresh time of 15 ms between the robot and the print head controller, the real-time synchronization of the tool translation speed and ink jetting frequency was not a viable solution for the high-speed printing (> 15 mm/s).

Thereafter, the method chosen in this study was based on the preliminary analysis of robot speed data and the subsequent adjustment of printing parameters.

A VAL3 program was written based on the Motion add-on to retrieve robot speed data.

The function used was `$getSpeedFbk(tTool)`, which returns the Cartesian speed of the TCP updated every 4 ms with each new feedback from the drives.

Conductive ink printing on planar and curved substrates

A solvent-based silver microparticle ink with density of 1.98 g/cm³ and 66.6 wt% dry content (Henkel, Loctite Edag 418SS, screen-printing ink) was used as received. After printing, the ink was dried in an air circulation oven for 30 min at a temperature of 90 °C.

Four planar substrates with different surface properties were used to investigate their contribution on printed lines geometry/conductivity:

- Two commercial sheets for flexible printed electronics: a 100 µm thickness PET sheet supplied by Lyreco (PET) and a coated paper, PowerCoat® (PC), supplied by Arjowiggins.
- A 80 g/m² and 113 µm thickness commercial printing–writing paper, supplied by Inapa (PW).
- A non-oriented paper sheet, 120 g/m² (HS), produced using bleached Kraft softwood fibres and a Rapid Khöten hand sheet former.

In order to determine the effect of the print speed and substrate on line width, height and electric resistance, step-shaped patterns were printed on each substrate at velocities and jetting frequencies ranging between 15 and 50 cm/s and 1 and 350 Hz, respectively.

The effect of drop superposition and substrate type on the printed pattern were also analysed under static conditions by depositing trains of 1 to 10 drops on the same point.

Printed patterns were characterised using a binocular magnifier Zeiss Stereo Discovery v20 equipped with a lens Zeiss Plan s 1.0x fwd 81.

The images were taken with a magnification factor x10. For PW and HS, observations were made in bright field, whereas for glossy PET and PC in dark fields. Images were then processed with a Python script using the OpenCV library. The width of the printed lines was obtained by calculating the distance between the upper edge and the lower edge pixel by pixel, and an average value was calculated for segments with a cumulative length of 5 cm.

The thickness of the printed patterns (i.e. drops or lines) was measured with an Alicona Infinite Focus 3D optical profilometer and their electric resistivity was calculated using the Ohm law and the electric resistance measured on 35 mm length control lines with 2 points probe and a digital multimeter (Fluke 113).

In order to test the validity of the freeform 3D printing process developed in this work, an interdigitated geometry was printed on the external surface of a commercial paper cup following the protocol illustrated in Figure 2. Algorithms for the object scan, 3D mesh reconstruction, 2D circuit projection on the 3D surface and robot motion analysis/speed segmentation were developed in the framework of this study, however they won't be detailed since they are outside the aim of this paper.

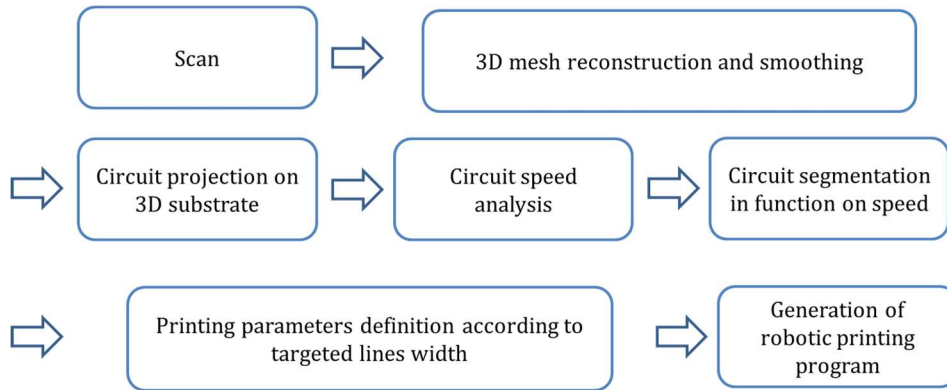


Figure 2. Unit operation implemented on the robot arm and printing protocol used to print conductive paths on a 3D substrate (i.e. a commercial paper cup).

THEORY AND EXPERIMENT

Printing velocity and line geometry/resistance

Ink droplets colliding to a planar surface are subjected to energy dissipation and surface forces which induce fluid splashing and spreading (Figure 3). Thereafter, the diameter of the equivalent circle of the deposited drop can be calculated using the general equation

$$D = S \cdot D_0 \quad (1)$$

where D_0 is the equivalent sphere diameter of the ejected ink drop (i.e. 287 μm in this study) and S is the drop spreading coefficient on the substrate.

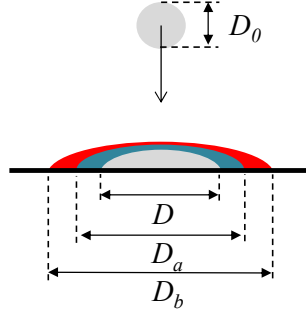


Figure 3. Scheme of ink drop impact and spreading over a flat surface. D_0 represents the equivalent sphere diameter of the ejected ink, D is the equivalent circle diameter of a unit droplet deposited on the substrate, D_a and D_b are the equivalent circle diameter of 5 and 10 superposed unit droplets.

Preliminary experimental data show that, despite the high ink viscosity,⁷ the equivalent circle diameter, and subsequently the spreading coefficient, can be affected by the number of drops (n_d) overlapping during the deposition process which can be calculated as:

$$n_d = \frac{D}{d} = \frac{1}{1-C} \quad (2)$$

where the distance between centers of adjacent drops (d) (Figure 1b) and the linear coverage ratio between deposited drops (C) are defined as

$$d = (DL + EL) \cdot V_T \quad (3),$$

$$C = \frac{D-d}{D} \quad (4),$$

and V_T is the translation speed of the print head and drop ejection time, EL and DL are the jetting- and rest-time (i.e. $DL + EL = T$, i.e. the drop jetting period).

Under the assumption of paths with linear edges, the equivalent line width (no spreading due to drop superposition) is given by the equation

$$w = \left\{ \frac{\pi D^2}{4} - \left[2 \cdot \frac{D^2}{4} \cdot \sin^{-1} \left(\frac{\sqrt{D^2 - d^2}}{D} \right) - \frac{d}{2} \cdot \sqrt{D^2 - d^2} \right] \right\} / d \quad (5)$$

and by using Eqs. 1 and 2 it can be written as

$$w = \frac{S \cdot D_0}{2} \cdot \left\{ \frac{\pi}{2 \cdot (1-C)} - \left[\frac{\sin^{-1} \sqrt{1 - (1-C)^2}}{1-C} - \sqrt{1 - (1-C)^2} \right] \right\} \quad (6).$$

When neglecting the generation of a curved meniscus between neighboring droplets, the minimum line width can be expressed as the cord between intersecting circles, i.e.:

$$w_{min} = D \cdot \text{Sin}\theta \quad (7),$$

where

$$\theta = \text{Cos}^{-1} \frac{d}{D} \quad (8).$$

In order to print continuous lines, a coverage ratio $C > 0$ is necessary and neighboring drops colliding on the substrate can go through partial to complete superposition ($C = 1$), thus affecting spreading and the final ink/substrate contact area. In order to account for this phenomenon, the ink spreading coefficient variation as a function of the coverage ratio was described by the hyperbolic function

$$S = \frac{S_0}{1-\alpha \cdot C^\beta} \quad (9)$$

where S_0 is the spreading coefficient of a unit ink drop and α and β are fitting coefficients. Eq. 9 was used to fit data obtained both under static-condition (i.e. superposition of a discrete number of drops) and, coupled to Eqs. 1 and 9 under dynamic-conditions (variation of the coverage ratio).

In order to estimate the line electric resistance, dry printed lines were assumed to have a semi elliptical profile and the cross section and peak height were calculated as

$$A = \frac{V_d}{D} \quad (10)$$

and

$$h = \frac{4 \cdot A}{\pi \cdot w} \quad (11)$$

where V_d is the dry ink volume deposited for a line length corresponding to a unit diameter (D)

$$V_d = V_0 \cdot n_d \cdot \frac{\rho_l}{\rho_d} \quad (12),$$

n_d is the corresponding number of deposited drops

$$n_d = \frac{D}{d} \quad (13),$$

V_0 is the drop unit volume, ρ_l and ρ_d are the liquid- and the dry-ink densities, respectively.

The resistance of printed lines was finally obtained using the Ohm's law

$$R = \frac{l}{\gamma \cdot A \cdot \sigma} \quad (14)$$

where σ is the ink electrical conductivity, i.e. $313 \pm 40 \times 10^6 \text{ S m}^{-1}$ for the Ag ink used in this study,⁷ l the line length, A the line geometric cross-sectional area and γ a correction factor accounting for defects/irregularities in the line cross section which can be correlated to the ration between the effective (A_{eff}) and the geometric (A) cross section, i.e. A_{eff}/A .

Analysis of tool head translation velocity

According to model Eqs. 1-14, the control of the tool head translation velocity V_T has a dominant role in affecting both the geometry and the electric resistance of printed lines. In order to evaluate velocity fluctuations of the 6-axis robot under well defined conditions, the robot tool head speed and position were collected along a step-shaped planar trajectory and retrieved in a .csv file. The trajectory was reconstructed in Rhinoceros 3D with a colour code corresponding to the speed variation (Figure 4).

In order to avoid a stop and go movement at each point, which would impair the printing process, the trajectory needs to be blended and angles smoothed. Thereafter, 3 speeds (15, 30 and 50 mm/s) and 3 blends (0.01, 0.1, and 1 mm) were tested and two printed patterns, composed by four adjacent step shape segments with angles smoothed with bending radii of 0 and 1 mm, were used. For each targeted speed, measurements were taken on the 4 trajectories. An analysis was made on 2D patterns to compare the speed fluctuations with the targeted speed. Hence, for each configuration, the exactitude, repeatability, and fluctuation were calculated according to ISO norm 9238. The exactitude of a trajectory speed, i.e. the error between the average and the target (controlled) speed obtained during n repetitions along the full trajectory, was calculated as follows:

$$E = \frac{v - v_c}{v_c} \cdot 100 \quad (15)$$

where $v = \frac{1}{n} \sum v_j$ is the arithmetic average speed over the full trajectory, $v_j = \frac{1}{m} \sum v_{ij}$ is the arithmetic average speed calculated over all measured values and v_c is the controlled speed. The repeatability of the trajectory speed, i.e. the closeness of agreement between the speeds achieved for the same controlled speed. Was expressed as a percentage of the controlled speed and calculated as follows:

$$R = \mp \left(\frac{3 S_v}{v_c} \cdot 100 \right) \quad (16)$$



Figure 4. Printing pattern and reconstructed trajectory as a function of speed. Nominal speed 30 mm/s, no blend, no angle smoothing. The green points correspond to a speed lower than the targeted speed (ca. 15 mm/min), the yellow points are close to the targeted speed, and the red points are higher than the targeted speed (ca. 20 mm/min).

$$\text{where } S_v = \sqrt{\frac{\sum (v_j - v)^2}{n-1}}.$$

The fluctuation of the trajectory speed is the maximum speed deviation during a cycle for a controlled speed. Fluctuation of trajectory speed (F) was calculated as the maximum deviation of the speed fluctuation for each cycle

$$F = [\max(v_{ij}) - \min(v_{ij})] \quad (17)$$

where v_{ij} is the speed achieved for the i measure and j cycle, and m is the number of measures along the trajectory.

RESULTS AND DISCUSSION

Correlating printing velocity to line geometry and resistance

Tested substrates were made of slightly polar polymers with similar surface energies (Table 1) but displayed radically different surface roughness, which ranged from 30, 100 nm of PET and PC to 11, 15 μm of PW and HS paper sheets.

Splashing and subsequent spreading of the ink drop led to dry ink dots with equivalent diameter progressively increasing with the substrate smoothness (Table 1).

According to the rheological behaviour of the silver ink used in this study, namely: i) a shear thinning and thixotropic behaviour⁷ characterized by a viscosity drop from 40 to 4 Pa.s when increasing the shear rate from 1 to 1000 s^{-1} , ii) a viscosity recovery after intense shearing requiring a time interval of few seconds, i.e. two-three orders of magnitude longer than the

timescale of processes involved in ink jetting, ink droplets splashing on the substrate hold a fluid behaviour. Nevertheless, the polar ink solvent (i.e. 2-Butoxyethoxy-ethanol, miscible with water and with a tension of 30 mN/m),¹⁸ quickly absorbs into porous substrates. On smooth and low porosity PET and PC, the ink solvent did not penetrate into the substrate and the ink hold a fluid behaviour. On rough and porous PW and HS, capillary forces were not sufficient to promote the whole ink penetration into paper porosity, whereas, the solvent selectively penetrated into the substrate thus increasing the ink dry solids content, its viscosity and freezing surface spreading. This phenomenon is well illustrated by the progressive decrease of unit drops spreading coefficient (S_0) from 2.2 to 1.53 when the substrate roughness increased from 0.03 to 15 μm (Table 1). A similar effect of substrate porosity was reported for ink jet printing on cellulosic membranes.¹⁹⁻²²

In addition to the unit drop contact diameter, which decreased from 632 to 440 μm when using PET or HS, drops deposited on PW and HS displayed an irregular asymmetric shape (Figure 5.b) which was ascribed to an anisotropic ink slip-stick spreading on rough surfaces.²² Ink drop on smooth PET and PC displayed an axisymmetric shape (Figure 5.b).

Substrate	PET	PC	PW	HS
SE (mN/m^2)	41 ¹⁹	32 ¹⁹	47-49 ^{19,21}	47-49 ^{19,21}
R_a (μm)	0.03	0.10	11	15
D_0 (μm)	632	580	480	440
h (μm)	15	18	40	42
S_0	2.2	1.95	1.67	1.53
α	0.75	0.75	0.75	0.75
β	2.20	2.20	2.20	2.20

Table 1. Substrate surface roughness (R_a), unit drop contact diameter (D)/peak height (h), unit drop spreading coefficient (S_0) and fitting coefficients of Equation 9 obtained from the interpolation of experimental data. A_{eff}/A represents the ratio between the effective and calculated conductive section of printed lines as obtained from line resistance measurements.

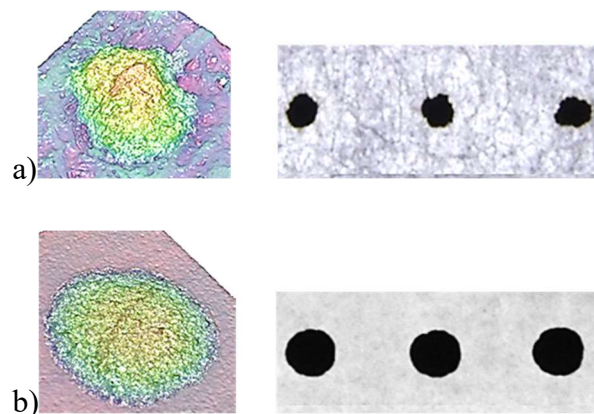


Figure 5. Examples of unit drops deposited on (a) rough PW and (b) smooth PC.

Figure 6 shows that similar morphologies were observed for continuous lines printed depositing drop trains with a coverage ratio of 50%. For all tested conditions, printed lines displayed semi-elliptical profiles and, as for single drops deposited under static conditions, the different ink spreading behaviour affected both lines profile ellipticity, which ranged from 0.83 to 0.95 for the PET-PC and the PW-HS substrates, and width. Figure 7a,b shows that, at a low coverage ratio of 30%, lines printed on PET display a nearly constant width and the absence of bridges between drops. Whereas, lines printed on rough PW with a 45% coverage ratio have irregular width and pronounced necking.

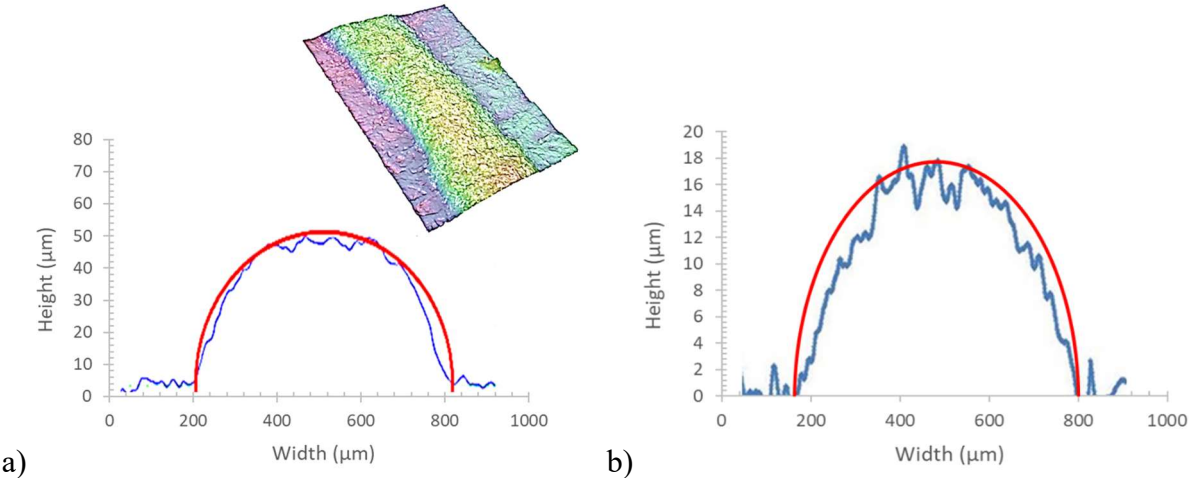


Figure 6. Cross section profile of Ag ink line printed on (a) PW with a coverage ratio of 80% and (b) PC with a coverage ratio of 50% and the corresponding semi-elliptical profile obtained with Eqs. (6) and (11).

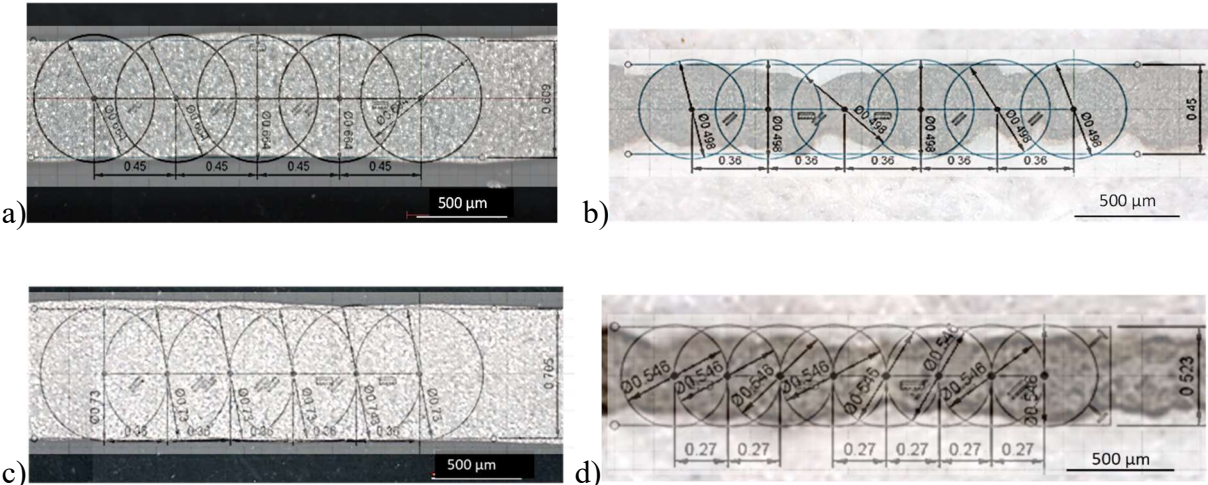


Figure 7. Ag ink lines printed on PET and PW with different coverage ratio. (a) PET substrate with a coverage ratio of 30%; (b) PW substrate with a coverage ratio of 45%; (c) PET substrate with a coverage ratio of 50%; (d) PW substrate with a coverage ratio of 60%.

As for individual drops, lines morphology was associated to the different solvent adsorption and drop spreading on smooth and rough substrates. As illustrated in Figure 7d, the increase of the coverage ratio from 45 to 60% slightly reduced line width fluctuations on PW, thus indicating that the increase of drop superposition poorly affects necking and line width variability. Solvent migration and surface roughness have a dominant effect on line geometry. Figure 8 shows that the increase of the drop coverage ratio led to an increase of the spreading coefficient (PET case in the inset of Figure 8a) and of the pattern/line width printed under static and dynamic conditions, respectively. Experimental line widths obtained for PET were in agreement with data predicted by with Eq. 6. Whereas, as the roughness of the printing substrate increased, experimental data progressively deviated from model predictions. The large scattering observed for PW and HS substrates (Figure 8c,d) was ascribed to the limited ink spreading and to presence of irregular and pronounced necks (Figure 7).

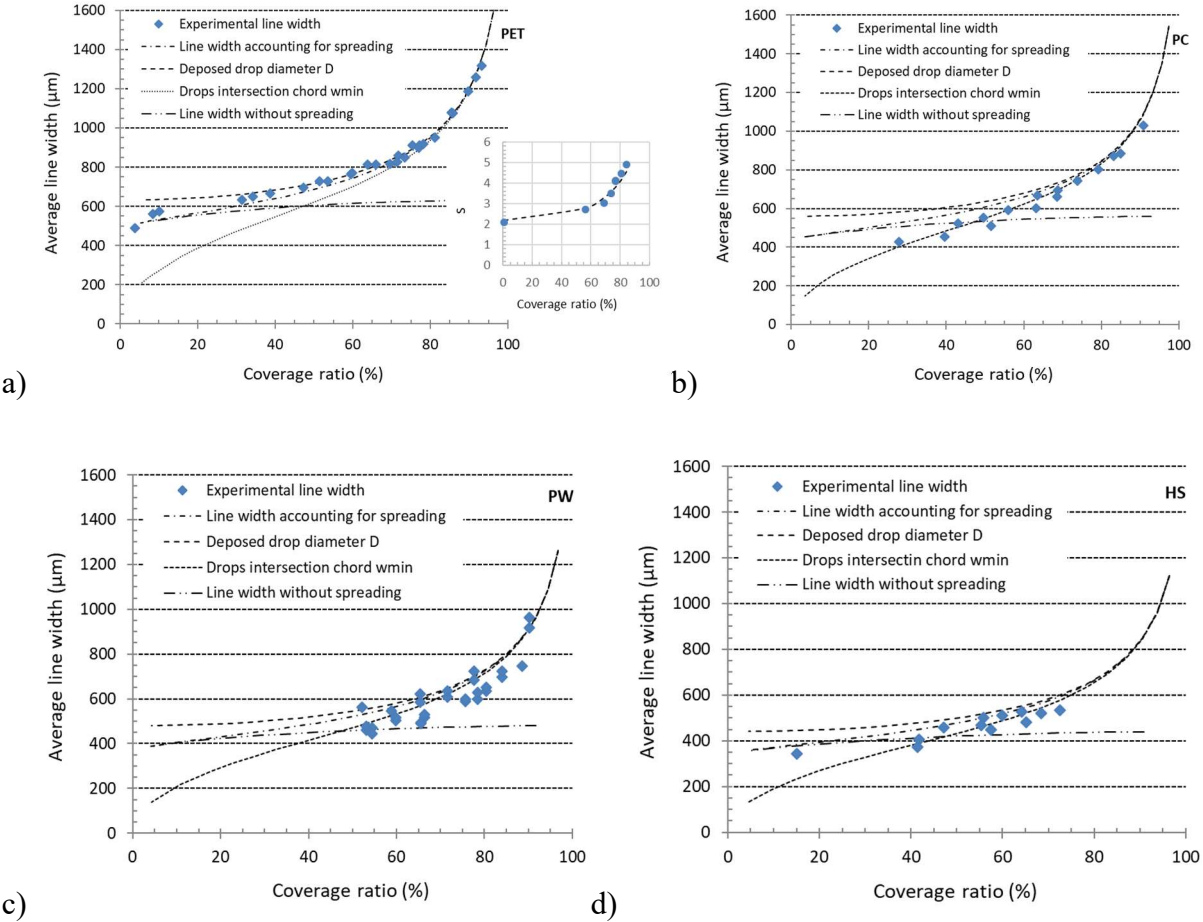


Figure 8. Experimental and calculated line width plotted as a function of substrate type and drop coverage ratio. PET (a), PC (b), PW (c) and HS (d) substrate.

Despite deviations up to 20% and scattered values, average line widths obtained for PW and HS followed with acceptable accuracy the trend predicted by Eq. 9, i.e. a progressive increase of line width when increasing the coverage ratio or when shifting from a rough to a smooth substrate bearing similar surface energy. Resistance values calculated for PET using Eqs. 9-14 for a line of 35 mm showed an excellent agreement with experimental data (Figure 9.a) and a unit A_{eff}/A ratio, thus confirming the regular geometry of conductive paths, i.e. nearly constant width with semi elliptical cross section. Figure 9 shows that the increase of rugosity in PC, PW and HS substrates, reduced ink spreading and necking led to printed lines with smaller average width and higher electric resistance. The irregular and low ink spreading on rough substrates was reflected by a drop in the effective line cross sectional area ratio A_{eff}/A obtained from experimental data fitting with Eqs. 9-14 which, as shown in Figure 9, progressively decreased from 1 to 0.9, 0.5 and 0.4 for lines printed on PET, PC, PW and HS, respectively. Trends observed in this study with a solvent based Ag paste are in line with the typical increase of necking and line resistance observed for ink jet printed lines on papers with increasing surface roughness.²³ Overall, the analysis of printed lines morphology and electric resistance allowed establishing direct correlations between printing variables (i.e. jetting frequency and print head translation speed), unit drop spreading on rough substrates and printed line width and electric resistance. Eqs. 1-14 and experimental data on unit drop diameter and spreading on various substrates given in Table 1 were integrated in the robot arm control software in order to synchronize the printhead translation speed and jetting frequency for a target line width and electric resistance.

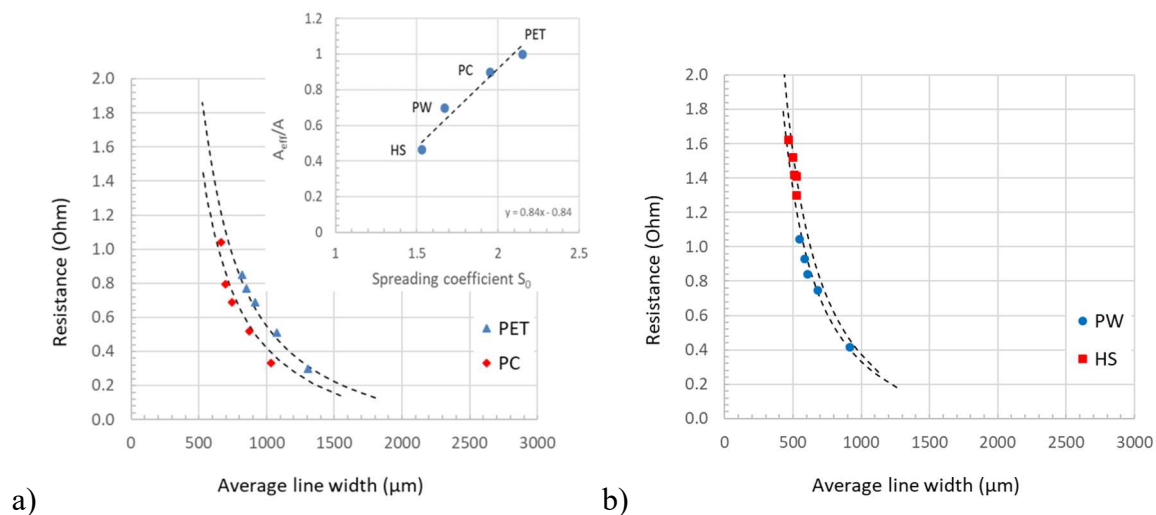
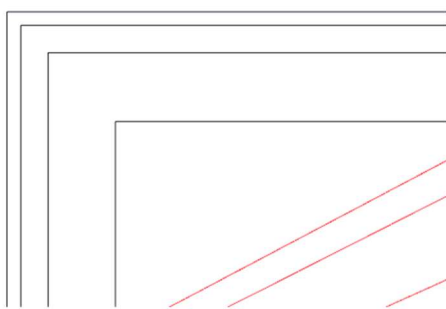


Figure 9. Resistance of a 35 mm printed line determined as a function of line width and substrate type. Dashed lines represent data fitting with Eqs. 10-14. (a) PET and PC substrates. The inset represents the ratio between the effective and the geometric cross section as obtained from data fitting with Eq. 14.

Speed variation analysis

The impact of the V_T speed variation on two 2D patterns (Angle Radius = 0 mm and Angle Radius = 1 mm) reported in Figures 10 and 11 show that speed exactitude and fluctuation over the test step-shape line are strongly affected by the target speed and the presence of sharp angles. Straight angle smoothing with a bending radius of 1 mm and blending reduce speed fluctuations along the trajectory. Nevertheless, they remain heterogeneously distributed along the printing path and attain minimum values of 5 and 20 mm/s for target speeds of 15 and 50 mm/s. Experimental data indicate that i) the speed control dictated by the 6-axis robot kinematics represents a bottleneck for high-speed ink dispensing and ii) V_T speed analysis along the printing trajectory and synchronization with the ink jetting frequency are necessary to control drop overlapping (i.e. the printed line geometry and resistance) along complex trajectories. The repeatability values are constant and low, around 0.01 %, regardless of the set of parameters. Consequently, the repeatability is independent of the targeted speed and blend.

Angle Radius = 0 mm

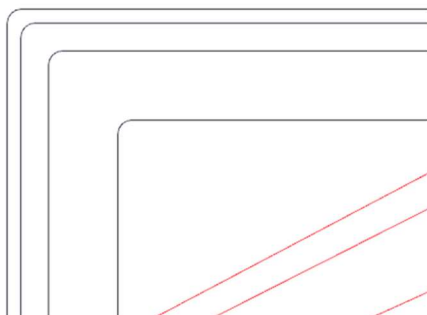


Angle Radius = 0 mm

Speed (mm/s)	Blend (mm)	Exactitude (%)	Repeatability (%)	Fluctuation (mm/s)
15	0,01	-0,72	0,01	8,456
	0,1	-0,26	0,01	8,377
	1	-0,23	0,01	7,545
30	0,01	-4,09	0,04	15,063
	0,1	-0,69	0,01	16,216
	1	-0,63	0,01	16,634
50	0,01	-10,56	0,02	24,103
	0,1	-1,9	0,01	28,506
	1	-0,94	0,01	20,608

Figure 10. Speed variation analysis with an angle radius of 0 mm.

Angle Radius = 1 mm



Angle Radius = 1 mm

Speed (mm/s)	Blend (mm)	Exactitude (%)	Repeatability (%)	Fluctuation (mm/s)
15	0,01	-0,629	0,01	7,579
	0,1	-0,14	0,01	7,008
	1	-0,14	0,01	5,779
30	0,01	-4	0,01	13,06
	0,1	-0,44	0,01	11,977
	1	-0,38	0,01	10,092
50	0,01	-10,61	0,02	25,528
	0,1	-1,56	0,02	21,784
	1	-0,94	0,01	20,608

Figure 11. Speed variation analysis with an angle radius of 1 mm.

3D circuit printing

As a representative case study, a 3D circuit was printed on a conical paper cup according to the protocol summarized in Figure 2. After scanning the printing substrate with the laser sensor to position the object in the robot working volume, the 3D mesh of the printing surface was generated (Figure 12) and a 2D circuit was projected on the 3D model.

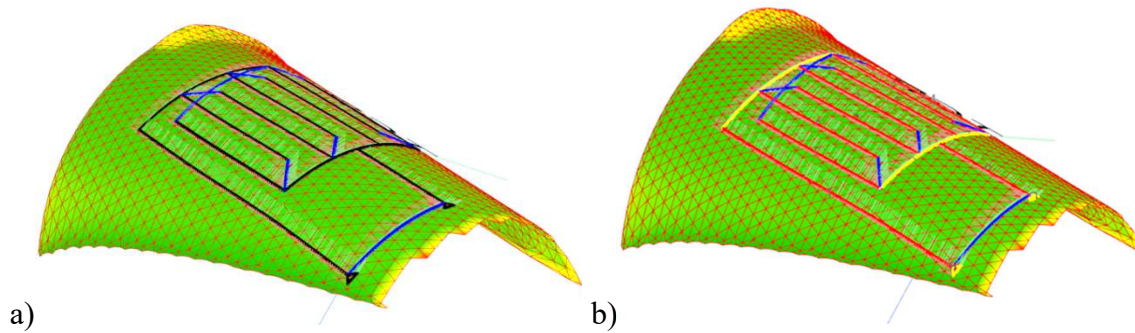


Figure 12. Circuit design (a) and trajectory representation in function of speed with a target speed of 15 mm/s (b).

Unit drops deposited on the paper cup had base diameter D of 500 μm (Table 2), similar to those obtained for PW and HS paper substrates. When the printing head was operated with a constant drop ejection frequency, the fluctuating translation velocity generated by the robot kinematics (which ranged between 7.5 and 14.5 mm/s for a target speed of 15 mm/s) and substrate roughness induced large variations in the line width. Depending on the local printhead velocity, line width varied from 475 to 660 μm (Figure 13). When compared to data predicted by Eqs. 1-14 using local velocities (Table 2) and a constant ejection frequency of 51 Hz, line width scattered of ca. 10 μm , indicating that model equations predicted with good accuracy the effect of printing velocity on lines shape on 3D. However, observed line width fluctuations were not compatible with the tolerance required to print electronic circuits highlighting the need for an accurate synchronization between the drop ejection rate and the printhead translation velocity. The slow refresh rate of the robot and printhead controllers of 250 and 60 Hz did not allow a real-time synchronization between the printhead translation velocity and the jetting rate. Thereafter, the printhead velocity along the working trajectory was retrieved during a first blank run and circuit segmentation was used to lower the line width variations, i.e. the circuit was divided into discrete segments with low speed fluctuation ($\sim 10\%$) and the average segment speed was used to synchronise the jetting rate of the printing head.

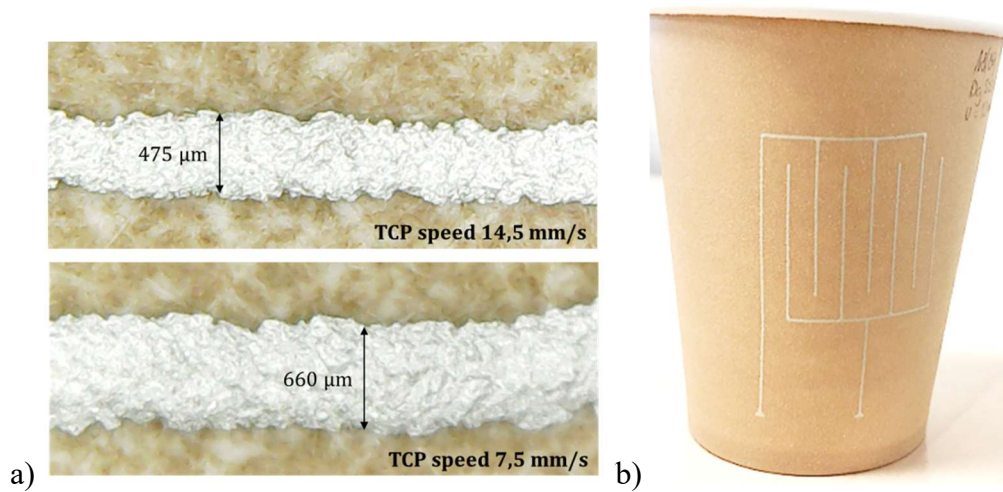


Figure 13. a) Printed line width for 50 % and with a constant DL of 19 ms. b) Printed circuit on paper cup with adjusted parameters.

V_T	D	DL	C	Predicted width	Measured width
mm/s	μm	ms	%	μm	μm
7.5	500	19	67.5	653	660
14.5	500	19	37.1	467	475

Table 2. Comparison between the measured and predicted line width with constant DL.

The local average speed, coverage ratio and the corresponding jetting frequency (i.e. jetting delay DL) were calculated as a function of the targeted line width (i.e. 525 μm) for each segment using Eqs. 1-6. The resistance of a 35 mm control line was estimated using Eq. 14.

As presented in Table 3, to have a circuit with constant line width, the delay DL was decreased from 32.5 to 14 ms for tool speeds of 7.1 and 15 mm/s and printed lines displayed width with and electric resistance in good agreement with values predicted by Eqs. 1-14 (Table 3).

V_T	D	DL	C	Predicted width	Predicted resistance*	Measured width	Measured resistance*
mm/s	μm	ms	%	μm	Ohm	μm	Ohm
7.1		32.5					
9	500	25.1	50	525	1.22	525 ± 10	1.60 ± 0.1
14.5		14.5					
15		14					

Table 3. Comparison between measured and predicted line width with adjusted DL *Electric resistance of a 35 mm control line.

CONCLUSION

This work demonstrates that a 6-axis industrial robot coupled with a piezo-jetting printhead and a semi empirical model to predict line width as a function of printing velocity and unit drop spreading can be conveniently used for the high-precision printing of a solvent-based silver on 3D substrates.

The analysis of the morphology and electric conductivity of silver ink lines printed on 2D substrates with different surface roughness (i.e. PET and different paper grades) showed that for the smooth PET substrate the line profile was dominated by the ink surface spreading which, even with an intermediate drop coverage ratio (i.e. 50%), induced the generation of thin and wide lines with minimal necking and low electric resistance (i.e. 16 μm , 680 μm and 1.14 Ohm for a 35 mm line). Whereas, the ink solvent penetration in porous paper substrates and an irregular drop spreading, induced the generation of thick and narrow lines with pronounced necking and higher electric resistance (i.e. 35 μm , 510 μm and 1.6 Ohm, respectively for rough paper hand sheets).

A semi empirical geometric model using the diameter of unit drops, the printing velocity and the ink jetting frequency was used to establish direct correlations between printed lines morphology, their electric resistance and printing parameters. The model was integrated in the 6-axis robot control software in order to adjust the ink jetting frequency as a function of a target line width/resistance and of the local printing velocity.

First printing tests on a 3D paper cup showed that the developed robotic cell and control software allow printing complete circuits with constant line width and electric resistance of ca. 525 μm and 1.6 Ohm (i.e. 24 mOhm/sq), thus minimizing the effect of speed fluctuations generated by the 6-axis kinematics on the circuit geometry.

AUTHOR INFORMATION

Authors contribution

The manuscript was written through contributions of all authors. All authors have given approval to the final version of the manuscript.

Funding sources

This work was supported by the Région Auvergne Rhône-Alpes (3DPap-EI project n° 17 011 070 01), the Institut Carnot PolyNat and the Laboratoire d'Excellence Tec21.

ACKNOWLEDGEMENTS

The authors would like to thank Dr. Denis Curtil and Mr. Philippe Lorent for their assistance in the configuration and assembly of the robotic cell.

REFERENCES

1. Berman, B. 3-D printing: The new industrial revolution. *Bus. Horiz.* **2012**, *55*, 155–162. <https://doi.org/10.1016/j.bushor.2011.11.003>.
2. Lewis, J. A.; Ahn, B. Y. Device fabrication: Three-dimensional printed electronics. *Nature* **2015**, *518*, 42–43. <https://doi.org/10.1038/518042a>.
3. Macdonald, E.; Salas, R.; Espalin, D.; Perez, M.; Aguilera, E.; Muse, D.; Wicker, R. B. 3D Printing for the Rapid Prototyping of Structural Electronics, *IEEE Access* **2014**, *2*, 234–242. <https://doi.org/10.1109/ACCESS.2014.2311810>.
4. Ledesma-Fernandez, J.; Tuck, C.; Hague, R. High viscosity jetting of conductive and dielectric pastes for printed electronics. *Proceed. of the Int. Solid Freeform Fab. Symp.* **2015**, 40-55.
5. Jia, H.; Hua, Z.; Li, M.; Zhang, J.; Zhang, J. A jetting system for chip on glass package, *Int. Conf. Electron. Packag. Technol. High Density Packag.* **2009**, pp. 954–960. <https://doi.org/10.1109/ICEPT.2009.5270564>.
6. Seifert, T.; Sowade, E.; Roscher, F.; Wiemer, M.; Gessner, T.; Baumann, R. R. Additive manufacturing technologies compared: morphology of deposits of silver ink using inkjet and aerosol jet printing. *Ind. & Eng. Chem. Res.* **2015**, *54*(2), 769-779.
7. Tricot, F.; Venet, C.; Beneventi, D.; Curtil, D.; Chaussy, D.; Vuong, T. P.; Broquin, J. E.; Reverdy-Bruas, N. Fabrication of 3D conductive circuits: print quality evaluation of a direct ink writing process. *RSC Adv.* **2018**, *8*, 26036–26046. <https://doi.org/10.1039/C8RA03380C>.
8. Roach, D. J.; Hamel, C. M.; Dunn, C. K.; Johnson, M. V.; Kuang, X.; Qi, H. J. The m4 3D printer: A multi-material multi-method additive manufacturing platform for future 3D printed structures. *Addit. Manuf.* **2019**, *29*, 100819. <https://doi.org/10.1016/j.addma.2019.100819>.
9. Urasinska-Wojcik, B.; Chilton, N.; Todd, P.; Elsworth, C.; Bates, M.; Roberts, G.; Gibbons, G. J. Integrated manufacture of polymer and conductive tracks for real-world applications. *Addit. Manuf.* **2019**, *29*, 100777. <https://doi.org/10.1016/j.addma.2019.06.028>.

10. Mitchell, A.; Lafont, U.; Hołyńska, M.; Semprimoschnig, C. Additive manufacturing — A review of 4D printing and future applications. *Addit. Manuf.* **2018**, *24*, 606–626. <https://doi.org/10.1016/j.addma.2018.10.038>.
11. Lorient, B. Automation of Acquisition and Post-processing for 3D Digitalisation. Theses, Université de Bourgogne, **2009**. <https://tel.archives-ouvertes.fr/tel-00371269> (accessed July 12, 2018).
12. Khalfaoui, S. Production automatique de modèles tridimensionnels par numérisation 3D, Dijon, **2012**. <http://www.theses.fr/2012DIJOS046> (accessed July 12, 2018).
13. Redinger, D.; Molesa, S.; Yin, S.; Farschi, R.; Subramanian, V. An ink-jet-deposited passive component process for RFID. *IEEE Trans. Electron Devices.* **2004**, *51*, 1978–1983. <https://doi.org/10.1109/TED.2004.838451>.
14. Subramanian, V.; Chang, J. B.; de la F. Vornbrock, A.; Huang, D. C.; Jagannathan, L.; Liao, F.; Mattis, B.; Molesa, S.; Redinger, D. R.; Soltman, D.; Volkman, S. K.; Zhang, Q. Printed electronics for low-cost electronic systems: Technology status and application development. *ESSCIRC 2008 - 34th Eur. Solid-State Circuits Conf.* **2008**, 17–24. <https://doi.org/10.1109/ESSCIRC.2008.4681785>.
15. Roth, Z.; Mooring, B.; Ravani, B. An overview of robot calibration. *IEEE J. Robot. Autom.* **1987**, *3*, 377–385. <https://doi.org/10.1109/JRA.1987.1087124>.
16. Khalil, W.; Dombre, E. Modeling, Identification and Control of Robots. Butterworth-Heinemann, **2004**.
17. Khalil, W.; Besnard, S. Geometric calibration of robots with flexible joints and links. *J. Intell. Robot. Syst.* **2002**, *34*, 357–379.
18. Dow Chemical Company. The Glycol Ethers Handbook. Midland, MI: Dow Chemical Co. **1990**, 97 pp.
19. Hoeng, F.; Bras, J.; Gicquel, E.; Krosnicki, G.; Denneulin, A. Inkjet printing of nanocellulose–silver ink onto nanocellulose coated cardboard. *Rsc Advances* **2017**, *7*(25), 15372-15381.
20. Saraiva, M. S.; Gamelas, J. A.; Mendes de Sousa, A. P.; Reis, B. M.; Amaral, J. L.; Ferreira, P. J. A new approach for the modification of paper surface properties using polyoxometalates. *Materials* **2010**, *3*(1), 201-215.
21. Clarke, A.; Blake, T. D.; Carruthers, K.; Woodward, A. Spreading and imbibition of liquid droplets on porous surfaces. *Langmuir* **2002**, *18*(8), 2980-2984.
22. Rosenholm, J. B. Liquid spreading on solid surfaces and penetration into porous matrices: Coated and uncoated papers. *Adv. Coll. Int. Sci.* **2015**, *220*, 8-53.

23. Ihalainen, P.; Määttänen, A.; Järnström, J.; Tobjörk, D.; Österbacka, R.; Peltonen, J.
Influence of surface properties of coated papers on printed electronics. *Ind. Eng. Chem. Res.* **2012**, *51*(17), 6025-6036.